

This manuscript has been authored by UT-Battelle, LLC under Contract No. DE-AC05-00OR22725 with the U.S. Department of Energy. The United States Government retains and the publisher, by accepting the article for publication, acknowledges that the United States Government retains a non-exclusive, paid-up, irrevocable, world-wide license to publish or reproduce the published form of this manuscript, or allow others to do so, for United States Government purposes. The Department of Energy will provide public access to these results of federally sponsored research in accordance with the DOE Public Access Plan (<http://energy.gov/downloads/doe-public-access-plan>).

Strong spin-dephasing in a topological insulator-paramagnet heterostructure

Jason Lapano¹, Alessandro R. Mazza¹, Haoxiang Li¹, Debangshu Mukherjee², Elizabeth M. Skoropata¹, Jong Mok Ok¹, Hu Miao¹, Robert G. Moore¹, Thomas Z. Ward¹, Gyula Eres¹, Ho Nyung Lee¹, Matthew Brahlek^{1*}

¹Materials Science and Technology Division, Oak Ridge National Laboratory, Oak Ridge, TN, 37831, USA

²Center for Nanophase Materials Sciences, Oak Ridge National Laboratory, Oak Ridge, TN, 37831, USA

Correspondence should be addressed to *brahlek@ornl.gov

Abstract: The interface between magnetic materials and topological insulators can drive the formation of exotic phases of matter and enable functionality through manipulation of the strong spin polarized transport. Here, we report that the spin-momentum-locked transport in the topological insulator Bi_2Se_3 is completely suppressed by scattering at a heterointerface with the kagome-lattice paramagnet, Co_7Se_8 . Bi_2Se_3 - Co_7Se_8 - Bi_2Se_3 trilayer heterostructures were grown using molecular beam epitaxy. Magnetotransport measurements revealed a substantial suppression of the weak antilocalization effect for Co_7Se_8 at thicknesses as thin as a monolayer, indicating a strong dephasing mechanism. $\text{Bi}_{2-x}\text{Co}_x\text{Se}_3$ films, where Co is in a non-magnetic 3^+ state, show weak antilocalization that survives to $x = 0.5$, which, in comparison with the heterostructures, suggests the unordered moments of the Co^{2+} act as a far stronger dephasing element. This work highlights several important points regarding spin-polarized transport in topological insulator interfaces and how magnetic materials can be integrated with topological materials to realize both exotic phases as well as novel device functionality.

Key Words: Topological insulator, molecular beam epitaxy, heterostructures, weak antilocalization

Topology has entered condensed matter physics and materials science as a classification scheme that distinguishes materials based upon a single number, the topological invariant¹. For the case of Z_2 topological insulators (TIs)², this invariant is determined by the ordering of the energy states of the band structure. At the boundary between 3-dimensional (3D) materials from different topological classes, new 2-dimensional (2D) singly degenerate energy states can emerge that possess linear Dirac-like dispersion and exhibit strong spin-momentum locked transport. These states can be modified by breaking time-reversal symmetry which gives many routes to control the surface state properties and electronic structure. Specifically, controllably opening a gap at the Dirac point can give rise to other exotic phases of topological matter, particularly, the quantized anomalous Hall phase³⁻⁷ as well as states that were envisioned in the realm of particle physics, for example axion phases⁸, which can be realized in condensed matter platforms. Due to these unique properties, the broad class of magnetic and topological materials are extremely promising for fundamental studies of exotic phases of matter as well as applications ranging from spintronics to quantum computing⁹⁻¹².

Numerous studies have focused on magnetically doping TIs to stabilize a ferromagnetic ground state¹³⁻¹⁷, which has resulted in the observation of the quantum anomalous Hall phase⁶. Combining TIs and magnetic materials as heterostructures offers an alternate route over bulk doping as magnetic coupling between the ferromagnetic material and a TI can be achieved without excessive scattering off random magnetic impurities¹⁸, as well as enabling the creation of distinct interfaces at the top and bottom surfaces, for example, which has been used to access axionic phases¹⁹⁻²¹. Specific questions remain regarding the fundamental scattering processes at interfaces between TIs and magnetic systems, particularly how the strong spin-momentum locking is modified in the presence of magnetic scattering centers and global magnetic ground states. Such questions are especially relevant for understanding interfaces with magnetic materials that are electrically insulating, for example yttrium iron garnet²² and $\text{Cr}_2\text{Ge}_2\text{Te}_6/\text{CrGeTe}_3$ ^{23,24}, as well as metallic interfaces such as permalloy and Pt²⁵. Here, we report that spin-momentum-locked transport in the TI Bi_2Se_3 is completely suppressed by scattering at the heterointerface with the kagome-lattice paramagnet, Co_7Se_8 . Despite time-reversal symmetry being fully intact, these results highlight the sensitivity of the spin-polarized transport at interfaces with strong moments. This dramatic effect raises the question whether the topological properties are fundamentally compromised at the Co_7Se_8 interfaces as well as the 2 remote interfaces between the Bi_2Se_3 and the surface and substrate: to answer this we show that the topology is intact at the surface using *in situ* angle-resolved photo-emission spectroscopy (ARPES). This work highlights the nontrivial interplay among magnetic and topological materials, which can be used to realize both exotic phases as well as novel device functionality.

Key to this study is utilizing molecular beam epitaxy (MBE) growth to create atomically sharp interfaces with the TI, here, Bi_2Se_3 and the kagome paramagnetic material Co_7Se_8 . Bi_2Se_3 is a prototypical topological insulator, having a relatively large band gap of 0.3 eV and a simple band structure with a single spin-polarized surface Dirac cone at the Γ point that is well separated from the 3D bulk bands²⁶⁻²⁸. As shown in the structural models in Fig. 1(a), the unit cell of Bi_2Se_3 is composed of three monolayers (ML) called quintuple layers (QL) that are roughly 1 nm thick. Co_7Se_8 has a monoclinic structure with a unit cell height of 0.52 nm, and 2 Co ML per unit cell. The Co_7Se_8 unit cell is characterized by an ordered-vacancy derivative of the hexagonal CoSe compound, in which 1/8 Co atoms are missing, creating alternating planes of close-packed hexagonal and kagome lattice structures²⁹, shown in Fig. 1(b). This yields Co with a mixed 2^+ and 3^+ valence state and a low-carrier density metal. Previous studies on bulk powder samples of Co_7Se_8 reported paramagnetism, and in nano-crystalline powders, trace amounts of Co or other Co-Se impurity phases can contribute to a weak ferromagnetic signature²⁹⁻³¹. However, MBE growth typically results in

highly uniform and homogeneous systems^{32,33}. These respective materials enable the application of strong magnetic disorder on the TI without breaking time reversal symmetry, which allows a cleaner view of the mechanisms driving the spin polarized transport. Trilayer structures used here were composed of a 7 QL Bi₂Se₃ bottom layer, a variable thickness Co₇Se₈ layer ranging in number of monolayers from $n = 1$ -23 ML, and a 7 QL Bi₂Se₃ top layer, as schematically shown in Fig. 1(c) along with a corresponding scanning transmission electron microscopy (STEM) image in Fig. 1(d). This structure was chosen since the bottom Bi₂Se₃ layer served as a necessary nucleation layer for Co₇Se₈, and the top Bi₂Se₃ layer preserved inversion symmetry between the Co₇Se₈ interfaces. Since the Bi₂Se₃ is in the regime where the bulk bands are occupied and the Co₇Se₈ is also metallic, both the top and bottom surface states can interact with the Co₇Se₈ through the free electrons in the bulk state of Bi₂Se₃. As such, this heterostructure enables probing both the nature of the spin-polarized transport as well as the topological character via ARPES on the top surface of the Bi₂Se₃.

Samples were grown using a home-built MBE system operating at a base pressure lower than 1×10^{-9} Torr. Cobalt, bismuth, and selenium were all supplied via thermal effusion cells. The source temperature of each cell was adjusted prior to growth to give the desired flux that was measured by a quartz crystal microbalance. Bi₂Se₃ and Co₇Se₈ were both grown in a self-regulated manner, where the flux ratios between the Bi:Se and Co:Se were around 1:10. As such, the Se shutter remained open during the entire growth sequence, whereas the growth of Bi₂Se₃ and a Co₇Se₈ were, respectively, controlled by timing the opening of the shutters based on the individual fluxes. Samples were grown on 5×5 mm² Al₂O₃ (0001) substrates, which were treated prior to growth with an acetone and IPA ultrasonic bath to degrease the surface, followed by annealing in air at 1000 °C. In all cases, an initial 2 QL Bi₂Se₃ buffer layer was deposited at 150 °C to maintain a smooth interface³⁴. The remainder of the heterostructures were grown at 200 °C, with the exception of the pure Bi₂Se₃ sample grown at 275 °C. Doped samples were grown by keeping the bismuth and selenium shutters open, while opening the Co shutter many times within a single monolayer to achieve homogeneous doping (see Fig. S1). X-ray diffraction measurements were performed on a Malvern Panalytical's X'Pert³ with a 4-circle goniometer using Cu $k_{\alpha 1}$ radiation. Transport measurements were performed in the van der Pauw geometry using pressed indium wires as contacts and measured in a Quantum Design Physical Property Measurement System down to a base temperature of 2 K. ARPES measurements were performed on a Scienta-Omicron ARPES system with a DA30-L electron analyzer, a helium lamp source with photon energy of 21.2 eV, and base temperature <10 K. The energy resolution of the ARPES measurement is 10 meV. Due to the difficulty in preserving the quality of the 2D materials during manual sample-preparation, STEM samples were thinned using a FEI Nova 200 focused ion beam (FIB), with the initial lift-out performed at an ion accelerating voltage of 30 kV, and final thinning performed at an accelerating voltage of 2 kV. Surface gallium ion implantation from the FIB thinning was removed by argon ion milling in a Fischione 1040 Nanomill, with 5 minutes per side at a voltage of 0.9 kV, which was followed by 1 minute of milling each side at 0.5 kV. The samples were subsequently imaged using a NION UltraSTEM 100 operating at an electron accelerating voltage of 100 kV, which was corrected for fifth order spherical aberrations. The images were collected using an annular dark field detector with the collection angles from 84-200 mrad. Images were collected with a pixel dwell time of 8 μ s. Overall beam exposure was minimal due to observed sensitivity to beam-damage.

To understand the global structure of the trilayer heterostructures, XRD measurements were performed to probe crystallinity, morphology, and interfacial character. 2θ - θ scans of the parent materials, Bi₂Se₃, and Co₇Se₈, as well as the trilayer heterostructures for various Co₇Se₈ thicknesses are shown in Fig. 2(a). The Bi₂Se₃ sample was 14 nm, the Co₇Se₈ was 10 nm, and for the trilayer heterostructures the Co₇Se₈

thickness ranged from $n = 1$ -23 ML. The 2θ - θ scan of Bi_2Se_3 shows the $003m$ series of peaks (m is an integer), which are highlighted by square-symbols. The peaks due to the Al_2O_3 substrate are marked with asterisks. Further, for the Bi_2Se_3 peaks Laue oscillations due to coherent scattering off the top and bottom interfaces can be seen about the most intense peaks, which indicates the films are extremely flat. The Co_7Se_8 film shows only the 001 and 002 reflections, as marked by circles. The lack of Laue oscillations indicate that the films are slightly rougher or, since the intensity of the oscillations scale with the intensity of the reflection, that they are below the scan's detection threshold due to the relative weakness of Co_7Se_8 001 and 002 peaks. The latter point is highlighted by comparing the 0012 reflection of Bi_2Se_3 at around $2\theta \approx 37^\circ$, which is similar magnitude at the 002 peak of Co_7Se_8 . Neither of these reflections show Laue oscillations, which indicates that the films are likely of similar flatness. The 2θ - θ scans of the trilayers samples, with Co_7Se_8 thickness ranging from $n = 1$ -23 ML, reveal a complex array of features. For the single monolayer the data looks very similar to Bi_2Se_3 , only with some of the reflections slightly distorted and with weak oscillations that are superimposed upon the main peaks. With increasing Co_7Se_8 -thickness, the Bi_2Se_3 peaks are further distorted, and these unusual oscillations become more prominent. Moreover, at 4 ML, the Co_7Se_8 peaks clearly emerge and by 23 ML are relatively sharp, which indicate that a significant portion of scattering emanates solely from Co_7Se_8 .

We further investigated the source of these intensity oscillations utilizing XRD simulations of the heterostructures for two plausible origins (see Supplementary Materials and Ref.[35] for additional details). For both cases, when the films are thick, interference should qualitatively occur if reflections from both the parent materials are close in 2θ . This occurs since the reflected X-rays can interfere constructively or destructively; away from these regions no coherent scattering should be seen. In the first scenario two pristine Bi_2Se_3 layers with sharp interfaces are separated by a thickness equivalent to n monolayers of Co_7Se_8 , representing an ideal structure, shown in Fig. 2(b) for the $n=8$ condition labelled "ideal 8 ML". This accounts for interference off the various interfaces, and clearly reproduces the experimental data. In the second scenario, we assume some interdiffusion of Co into the Bi_2Se_3 and perhaps Bi into the Co_7Se_8 which will likely occur asymmetrically if the $\text{Bi}_2\text{Se}_3/\text{Co}_7\text{Se}_8$ interface is different than the subsequent $\text{Co}_7\text{Se}_8/\text{Bi}_2\text{Se}_3$ interface^{33,36}. This would be accompanied by a modification of the out-of-plane lattice parameter in the various layers³⁷, thus creating, for example, peak broadening or multiple Bi_2Se_3 reflections very close in 2θ depending on the degree of lattice distortion and cobalt interdiffusion. However, interference should only occur at lower 2θ where the overlap of the reflections would be maximum and would give way to a splitting of the peaks at higher 2θ . This is shown in the simulation in Fig. 2(b) labeled "slightly mixed" and "heavily mixed", where the intensity is calculated for a bilayer structure composed of two Bi_2Se_3 of slightly different out-of-plane lattice parameters. For the lightly mixed case, a small (1%) variation in the lattice constant from the bulk Bi_2Se_3 reproduced the reflections at high 2θ values, but not the interference pattern at lower 2θ . For the heavily mixed sample which had a larger (5%) variation in the lattice constant, there is some interference at low 2θ values but a large degree of peak splitting at high 2θ . Moreover, X-ray photoelectron spectroscopy (XPS) was carried out on the trilayer with $n = 8$ ML and doped samples and is shown in Fig. S2. No cobalt signature could be seen for the trilayer sample, confirming that there is minimal diffusion of Co into the Bi_2Se_3 layers and that the surface is free of Co impurities. As such, this scenario can be eliminated. Considering this and returning to the experimental data in Fig. 2(a), comparing the trilayer structures to the simulated data reveals only the ideal case closely matches the experimental data at both high and low 2θ values, confirming the global structural quality of the trilayer heterostructures.

Now that the structural quality has been confirmed, we move on to magnetotransport measurements. Conductance versus magnetic field is shown in Fig. 3(a) for the trilayer samples in comparison to the 14 nm Bi₂Se₃ (0 ML) film measured at 2 K. With increasing magnetic field, the conductance for the Bi₂Se₃ sample shows a sharp drop with increasing field; at higher fields the conductance transitions to a weak B^2 dependence, where B is the magnetic field, which is characteristic of the free-electron response. For the trilayer heterostructures, the sharp drop in the conductance is substantially suppressed even for samples with Co₇Se₈ thickness as thin as a single monolayer, and by 4 ML the conductance exhibits solely a B^2 dependence. Transport in TIs in low magnetic field is characterized by a sharp cusp-like feature centered around $B = 0$ T³⁸. The origin of this feature, called weak antilocalization (WAL), is due to the magnetic field suppressing coherent backscattering. In TIs specifically, and, more generally, 2D systems with strong spin-orbit coupling, WAL is due to a reduction of the probability to backscatter, which is driven by the accumulation of phases of opposite sign for clockwise and counter-clockwise backscattering loops³⁹. Application of a small magnetic field, therefore, suppresses this effect, which is manifest as a sharp drop in conductance. The WAL effect can be quantified by fitting the experimental data using the Hikami-Larkin-Nagaoka (HLN) model for the change in conductance,

$$\Delta G(B) = \alpha \left(\frac{e^2}{2\pi h} \right) \left[\ln \left(\frac{B_\phi}{B} \right) - \Psi \left(\frac{1}{2} + \frac{B_\phi}{B} \right) \right] \quad (1)$$

in which $\Psi(x)$ is the digamma function, h is Planck's constant, e is the electron charge, and the two free parameters are α which quantifies the number of 2D channels (1 per channel; this has been rescaled by $1/(2\pi)$ relative to the original HLN formulation), and B_ϕ is the dephasing magnetic field⁴⁰. The dephasing magnetic field is related to the phase coherence length l_ϕ by the following equation.

$$B_\phi = \frac{\hbar}{4el_\phi^2} \quad (2)$$

The data was fit using the HLN model with an additional B^2 term to account for the free electron response. The fits are shown in Fig. 3(a) as solid lines for the Bi₂Se₃ and the trilayer with $n = 1$. The resulting l_ϕ and α are plotted versus Co₇Se₈ thickness in Fig. 3(b) and (c), respectively. For larger thicknesses, the low-field kink was absent, and, therefore, we took both l_ϕ and α to be zero indicating that there is no spin-polarized transport. The complete quenching of this effect is surprising since the transport for TIs should be immune from such scattering events so long as time reversal symmetry is intact. This immunity is demonstrated by the magnetoconductance data shown in Fig. 3(d). This data was taken from Bi_{2-x}Co_xSe₃ where x ranged from 0.07 to 0.50. For these films it is assumed that Co takes a non-magnetic 3⁺ valence state and predominately replaces Bi³⁺. Over this range the WAL effect can be seen clearly to survive to the highest doping range as the cusp in the conductance in the low field regime is maintained. Fitting to the HLN function shows that α is nominally constant and l_ϕ drops relative to the undoped materials.

To understand the data for both the trilayer structures and doped samples it is instructive to compare length scales for the scattering processes. For the trilayer samples scattering off the Co₇Se₈ layer provides complete dephasing, thus, the minimum length scale is then set by the Bi₂Se₃ thickness. Physically this implies that all backscattering loops that contribute to WAL effect contain at least one scattering event off the Co₇Se₈ layer. For Bi₂Se₃, where both the bulk and the surface states contribute to the WAL effect, scattering off the surfaces does not provide a dephasing mechanism, since WAL is observed from the thick limit of hundreds of nanometers down to the thin limit where surface scattering dominates the

resistance^{38,41,42}; moreover, in $\text{Bi}_2\text{Se}_3/(\text{Bi}_{1-x}\text{In}_x)_2\text{Se}_3/\text{Bi}_2\text{Se}_3$ trilayer heterostructures, there is a strong dependence on the doping levels and thickness of the $(\text{Bi}_{1-x}\text{In}_x)_2\text{Se}_3$ ⁴³. In contrast to this, in $\text{Bi}_{2-x}\text{Co}_x\text{Se}_3$, the length scale is approximately set by the average spacing of the dopants, which is of the order of a few nanometers for $x \approx 0.1$. Therefore, scattering due to Co defects should occur at a significantly higher rate than scattering off the Co_7Se_8 interfaces in the trilayer heterostructures. Yet, WAL is clearly observed for the highest doped samples. It is emphasized that the Co should be in a 3^+ valence state with no net moment. This highlights the extreme sensitivity of the spin-polarized transport processes to magnetic defects.

As the spin-polarized transport is fully suppressed, the question arises whether the trilayer system is topological. To answer this question *in situ* ARPES was performed on a trilayer sample with a Co_7Se_8 thickness of 8 ML at low temperature (<10 K). The spectrum for this sample is shown on the left of Fig. 4 (a). From this the linearly dispersive topological surface band is visible. This, and the degenerate Dirac point (DP), can be more clearly seen by processing the spectrum with the curvature method described in Ref. [44], as shown on the right-hand side of Fig. 4(a) and the equipotential map at various energies shown in Fig. 4(b). To further illustrate the gapless nature of the DP, we plot the stacking energy distribution curves (EDCs) in Fig. 4(c). The red curve indicates the EDC at $k_x = 0$, which shows a single peak at ~ 300 meV that corresponds to the DP position in the 2D spectrum in Fig. 4(a). However, the ARPES measurement only probes the top surface of the trilayer heterostructure. The electronic structure of the interface between Co_7Se_8 and Bi_2Se_3 remains uncertain. This, however, motivates the future question regarding the nature of the states that form at the interfaces of Co_7Se_8 . The strong magnetic moments of the Co will certainly interfere with the spin polarized states, but strong hybridization among the Co_7Se_8 states and the topological surface states may also inhibit its formation entirely. Since this interface is well below the escape depth for photoelectrons used here, this question will have to be addressed in the future in combination with first principles calculations.

To conclude, we have shown that spin-polarized transport is completely suppressed in the topological material Bi_2Se_3 by embedding an epitaxial layer of a kagome-paramagnetic material, Co_7Se_8 , using MBE growth. Scattering off the magnetic Co^{2+} in the Co_7Se_8 is the primary source of the strong spin dephasing. This is in stark contrast to $\text{Bi}_{2-x}\text{Co}_x\text{Se}_3$ where spin polarized transport is found to survive the non-magnetic disorder due to Co^{3+} even in doping levels as high as $x = 0.5$. *In situ* ARPES measurements show that, despite the absence of spin polarized transport, the topological band structure on the top surface remains intact. Taken with a broader perspective, the current measurements have deep implications. One of the biggest impacts comes from device functionality that relies on spin-polarization. Topological materials are supposed to be immune to disorder that obeys time reversal symmetry. Although Co_7Se_8 is not magnetic, it does have a net moment which causes complete spin dephasing of the charge carriers. As such, this demonstrates that in a device the materials need to be carefully chosen to avoid anything with a net moment—specifically, paramagnetic substrates with a net moment should be avoided for the growth of topological materials. Alternatively, if control over spin dephasing is desired, strong moment materials such as Co_7Se_8 can be incorporated epitaxially with TIs. Further questions regarding the source of dephasing in topological systems necessitates understanding and quantifying the dependence of the scattering processes on the details of the interfaces. As an example, metallic materials with a net moment, like Co_7Se_8 , may be more susceptible to suppressing spin-polarized transport processes than an insulating material with net moments. As such, proposals for realizing novel topological phases necessitate interfacing magnetic metals, insulators, or both, thus highlighting the significance of these questions. This work brings about a broader view of spin polarized transport processes in topological materials, which is significant for realizing novel phases of matter at topological interfaces and for engineering topological devices.

Supplementary Materials

See [supplementary materials](#) for additional X-ray diffraction data, details regarding the simulations, and X-ray photoemission spectroscopy.

Acknowledgements

This work was supported by the U.S. Department of Energy (DOE), Office of Science, Basic Energy Sciences, Materials Sciences and Engineering Division (transport, structural characterization, and MBE growth) and by the Laboratory Directed Research and Development Program of Oak Ridge National Laboratory, managed by UT-Battelle, LLC, for the U.S. DOE under Contract No. DE-AC05-00OR22725 (ARPES measurements). The electron microscopy work was conducted as a user project at the Center for Nanophase Materials Sciences, which is a U.S. DOE Office of Science User Facility.

AIP Publishing data sharing policy

The data that support the findings of this study are available from the corresponding author upon reasonable request.

References

- ¹ M.Z. Hasan and C.L. Kane, *Rev. Mod. Phys.* **82**, 3045 (2010).
- ² J.E. Moore and L. Balents, *Phys. Rev. B* **75**, 121306 (2007).
- ³ C.-X. Liu, S.-C. Zhang, and X.-L. Qi, *Annu. Rev. Condens. Matter Phys.* **7**, 301 (2016).
- ⁴ F.D.M. Haldane, *Phys. Rev. Lett.* **61**, 2015 (1988).
- ⁵ C.X. Liu, X.L. Qi, X. Dai, Z. Fang, and S.C. Zhang, *Phys. Rev. Lett.* **101**, 146802 (2008).
- ⁶ C.Z.C.-Z. Chang, J. Zhang, X. Feng, J. Shen, Z. Zhang, M. Guo, K. Li, Y. Ou, P. Wei, L.L.L.-L. Wang, Z.Q.Z.-Q. Ji, Y. Feng, S. Ji, X.X. Chen, J. Jia, X.X. Dai, Z. Fang, S.-C.S.C. Zhang, K. He, Y. Wang, L.L. Lu, X.-C.X.C. Ma, and Q.-K.Q.K. Xue, *Science* **340**, 167 (2013).
- ⁷ Y. Deng, Y. Yu, M.Z. Shi, Z. Guo, Z. Xu, J. Wang, X.H. Chen, and Y. Zhang, *Science* **367**, 895 (2020).
- ⁸ F. Wilczek, *Phys. Rev. Lett.* **58**, 1799 (1987).
- ⁹ M. He, H. Sun, and Q.L. He, *Front. Phys.* **14**, 43401 (2019).
- ¹⁰ L. Šmejkal, Y. Mokrousov, B. Yan, and A.H. MacDonald, *Nat. Phys.* **14**, 242 (2018).
- ¹¹ Y. Fan and K.L. Wang, *SPIN* **6**, (2016).
- ¹² S. Das Sarma, M. Freedman, and C. Nayak, *Npj Quantum Inf.* **1**, 15001 (2015).
- ¹³ W. Liu, L. He, Y. Xu, K. Murata, M.C. Onbasli, M. Lang, N.J. Maltby, S. Li, X. Wang, C.A. Ross, P. Bencok, G. van der Laan, R. Zhang, and K.L. Wang, *Nano Lett.* **15**, 764 (2015).
- ¹⁴ J.M. Zhang, W. Ming, Z. Huang, G. Bin Liu, X. Kou, Y. Fan, K.L. Wang, and Y. Yao, *Phys. Rev. B* **88**, 235131 (2013).

- ¹⁵ M. Liu, J. Zhang, C.-Z. Chang, Z. Zhang, X. Feng, K. Li, K. He, L. Wang, X. Chen, X. Dai, Z. Fang, Q.-K. Xue, X. Ma, and Y. Wang, *Phys. Rev. Lett.* **108**, 036805 (2012).
- ¹⁶ P.P.J. Haazen, J.B. Laloë, T.J. Nummy, H.J.M. Swagten, P. Jarillo-Herrero, D. Heiman, and J.S. Moodera, *Appl. Phys. Lett.* **100**, 082404 (2012).
- ¹⁷ W. Wang, Y. Ou, C. Liu, Y. Wang, K. He, Q.K. Xue, and W. Wu, *Nat. Phys.* **14**, 791 (2018).
- ¹⁸ V.N. Men'shov, V. V. Tugushev, S. V. Eremeev, P.M. Echenique, and E. V. Chulkov, *Phys. Rev. B* **88**, 224401 (2013).
- ¹⁹ M. Mogi, M. Kawamura, A. Tsukazaki, R. Yoshimi, K.S. Takahashi, M. Kawasaki, and Y. Tokura, *Sci. Adv.* **3**, 1669 (2017).
- ²⁰ D. Xiao, J. Jiang, J.H. Shin, W. Wang, F. Wang, Y.F. Zhao, C. Liu, W. Wu, M.H.W. Chan, N. Samarth, and C.Z. Chang, *Phys. Rev. Lett.* **120**, 056801 (2018).
- ²¹ C. Liu, Y.Y. Wang, H. Li, Y. Wu, Y. Li, J. Li, K. He, Y. Xu, J. Zhang, and Y.Y. Wang, *Nat. Mater.* **1** (2020).
- ²² Y.T. Fanchiang, K.H.M. Chen, C.C. Tseng, C.C. Chen, C.K. Cheng, S.R. Yang, C.N. Wu, S.F. Lee, M. Hong, and J. Kwo, *Nat. Commun.* **9**, 223 (2018).
- ²³ M. Mogi, T. Nakajima, V. Ukleev, A. Tsukazaki, R. Yoshimi, M. Kawamura, K.S. Takahashi, T. Hanashima, K. Kakurai, T.H. Arima, M. Kawasaki, and Y. Tokura, *Phys. Rev. Lett.* **123**, 016804 (2019).
- ²⁴ X. Yao, B. Gao, M.G. Han, D. Jain, J. Moon, J.W. Kim, Y. Zhu, S.W. Cheong, and S. Oh, *Nano Lett.* **19**, 4567 (2019).
- ²⁵ A.R. Mellnik, J.S. Lee, A. Richardella, J.L. Grab, P.J. Mintun, M.H. Fischer, A. Vaezi, A. Manchon, E.A. Kim, N. Samarth, and D.C. Ralph, *Nature* **511**, 449 (2014).
- ²⁶ H. Zhang, C.-X. Liu, X.-L. Qi, X. Dai, Z. Fang, and S.-C. Zhang, *Nat. Phys.* **5**, 438 (2009).
- ²⁷ H. Peng, K. Lai, D. Kong, S. Meister, Y. Chen, X.-L. Qi, S.-C. Zhang, Z.-X. Shen, and Y. Cui, *Nat. Mater.* **9**, 225 (2010).
- ²⁸ D. Hsieh, Y. Xia, D. Qian, L. Wray, J.H. Dil, F. Meier, J. Osterwalder, L. Patthey, J.G. Checkelsky, N.P. Ong, A. V. Fedorov, H. Lin, A. Bansil, D. Grauer, Y.S. Hor, R.J. Cava, and M.Z. Hasan, *Nature* **460**, 1101 (2009).
- ²⁹ F. Javier García-García, A.-K. Larsson, L. Norèn, and R.L. Withers, *Solid State Sci.* **6**, 725 (2004).
- ³⁰ V.L. Miller, W.-L. Lee, G. Lawes, N.-P. Ong, and R.J. Cava, *J. Solid State Chem.* **178**, 1508 (2005).
- ³¹ H. Ikeda, M. Shirai, N. Suzuki, and K. Motizuki, *J. Magn. Mater.* **159** (1995).
- ³² A.A. Taskin, S. Sasaki, K. Segawa, and Y. Ando, *Adv. Mater.* **24**, 5581 (2012).
- ³³ N. Koirala, M. Brahlek, M. Salehi, L. Wu, J. Dai, J. Waugh, T. Nummy, M.-G. Han, J. Moon, Y. Zhu, D. Dessau, W. Wu, N.P. Armitage, and S. Oh, *Nano Lett.* **15**, 8245 (2015).
- ³⁴ N. Bansal, Y.S. Kim, E. Edrey, M. Brahlek, Y. Horibe, K. Iida, M. Tanimura, G.-H. Li, T. Feng, H.-D. Lee, T. Gustafsson, E. Andrei, and S. Oh, *Thin Solid Films* **520**, 224 (2011).
- ³⁵ P.F. Miceli, *Semiconductor Interfaces, Microstructures and Devices: Properties and Applications* (IOP

Publishing, Bristol, 1993).

³⁶ H.D. Lee, C. Xu, S.M. Shubeita, M. Brahlek, N. Koirala, S. Oh, and T. Gustafsson, *Thin Solid Films* **556**, 322 (2014).

³⁷ M. Zhang, L. Lü, Z.-T. Wei, X.-S. Yang, and Y. Zhao, *Chinese Phys. B* **23**, 76104 (2014).

³⁸ M. Brahlek, N. Koirala, N. Bansal, and S. Oh, *Solid State Commun.* **215–216**, 54 (2015).

³⁹ K. Barnham and D.D. (Dimitri D. Vvedensky, *Low-Dimensional Semiconductor Structures : Fundamentals and Device Applications* (Cambridge University Press, 2001).

⁴⁰ S. Hikami, A.I. Larkin, and Y.O. Nagaoka, *Prog. Theor. Phys* **63**, (1980).

⁴¹ Y.S. Kim, M. Brahlek, N. Bansal, E. Edrey, G.A. Kapilevich, K. Iida, M. Tanimura, Y. Horibe, S.W. Cheong, and S. Oh, *Phys. Rev. B* **84**, 073109 (2011).

⁴² N. Bansal, Y. Seung Kim, M. Brahlek, E. Edrey, and S. Oh, (2012).

⁴³ M.J. Brahlek, N. Koirala, J. Liu, T.I. Yusufaly, M. Salehi, M.-G. Han, Y. Zhu, D. Vanderbilt, and S. Oh, *Phys. Rev. B* **93**, 125416 (2016).

⁴⁴ P. Zhang, P. Richard, T. Qian, Y.-M. Xu, X. Dai, and H. Ding, *Rev. Sci. Instrum.* **82**, 43712 (2011).

Figures

Fig. 1. Materials and experimental schematic. (a) Crystal structure of TI Bi_2Se_3 showing the layered hexagonal structure consisting of 3 repeated quintuple layer (QL) units of Se-Bi-Se-Bi-Se, three of which make the unit cell. (b) Co_7Se_8 is characterized by an ordered vacancy structure forming a kagome network of Co atoms in layer 1 and a hexagonal structure in layer 2. This leads to a mixed valence of 2^+ and 3^+ states, which are shown at the bottom decorating the layers as red arrows and blue circles, respectively. The structure is formally monoclinic, however the $\langle 1\bar{1}0 \rangle$ can be thought of as the pseudohexagonal $\langle 010 \rangle$ direction, showing the hexagonal arrangement between the two unit cells. (c-d) Schematic of the trilayer structure (c) and accompanying scanning high-angle annular dark field (HAADF) scanning transmission electron microscopy (STEM) image (d) for a Bi_2Se_3 (7 QL)/ Co_7Se_8 (23 ML)/ Bi_2Se_3 (7 QL) trilayer sample.

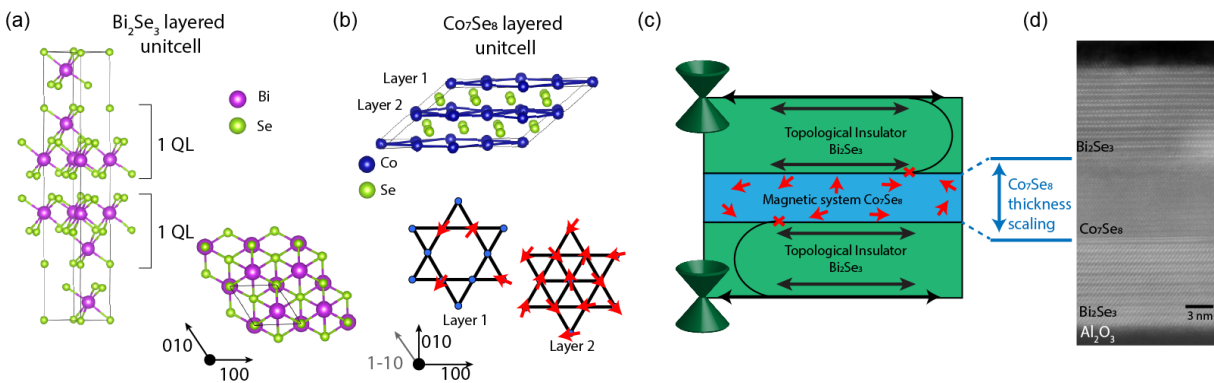


Fig. 2. X-ray diffraction (XRD) measurements and simulations of trilayer heterostructures and parent materials. (a) XRD 2θ - θ scans of the parent materials Bi_2Se_3 and Co_7Se_8 as well as trilayer heterostructures with Co_7Se_8 thickness ranging from $n = 1$ -23 monolayers (ML). The Bi_2Se_3 peaks are marked by square-symbols, Co_7Se_8 peaks are marked by circles, and the Al_2O_3 peaks are marked by asterisks. (b) Results from simulated structures including single-layer Bi_2Se_3 , bi-layer Bi_2Se_3 with differing c -axis lattice parameters labeled “lightly mixed” and “heavily mixed” (the expected splitting at large 2θ is labeled “ $\Delta 2\theta$ ”), as well as a Bi_2Se_3 heterostructure with spacing equivalent to 8 ML of Co_7Se_8 labeled “ideal 8 ML” (see Supplement Materials). X-ray diffraction of the doped samples can be found in Fig. S1.

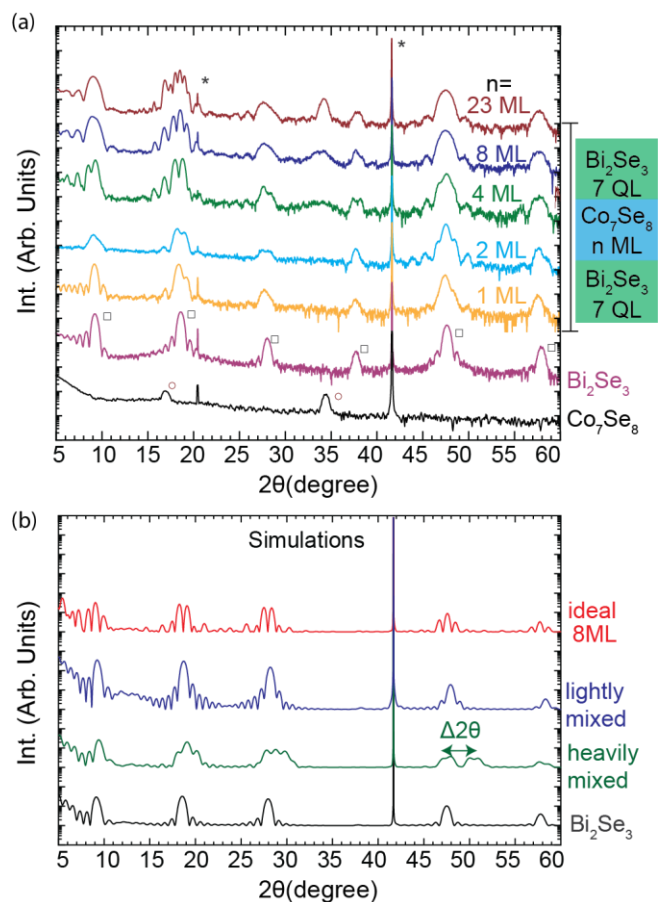


Fig. 3. Conductance versus magnetic field for trilayer heterostructures and doped samples. (a,d) Change in conductance versus magnetic field for the trilayer heterostructures (a) and for $\text{Bi}_{2-x}\text{Co}_x\text{Se}_3$ (d) where the data is shown as symbols and fit is the solid lines. Curves are offset for clarity. (b-c,e-f) Extracted α (number of conductance channels) and l_ϕ (phase coherence length) parameters from the HLN model are plotted for the trilayers (b-c) and $\text{Bi}_{2-x}\text{Co}_x\text{Se}_3$ (e-f), respectively. The single Bi_2Se_3 layer is the black square symbol, the trilayer are blue triangles, and the $\text{Bi}_{2-x}\text{Co}_x\text{Se}_3$ are the red circles. The dashed lines are guides-to-the-eye.

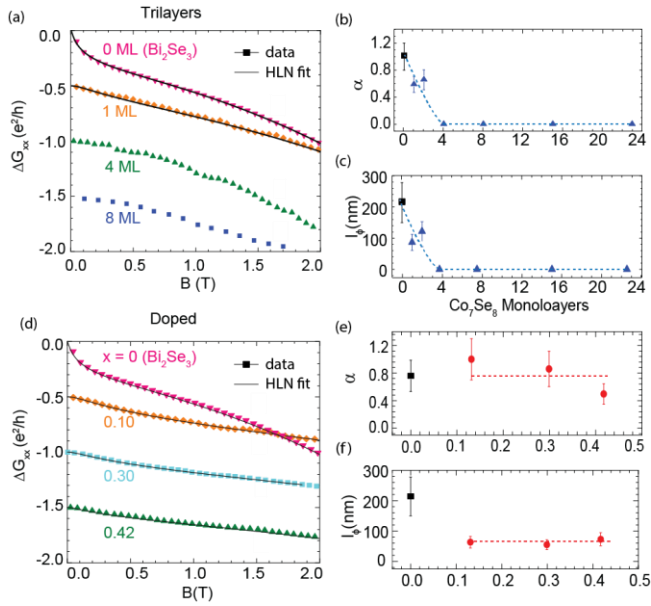
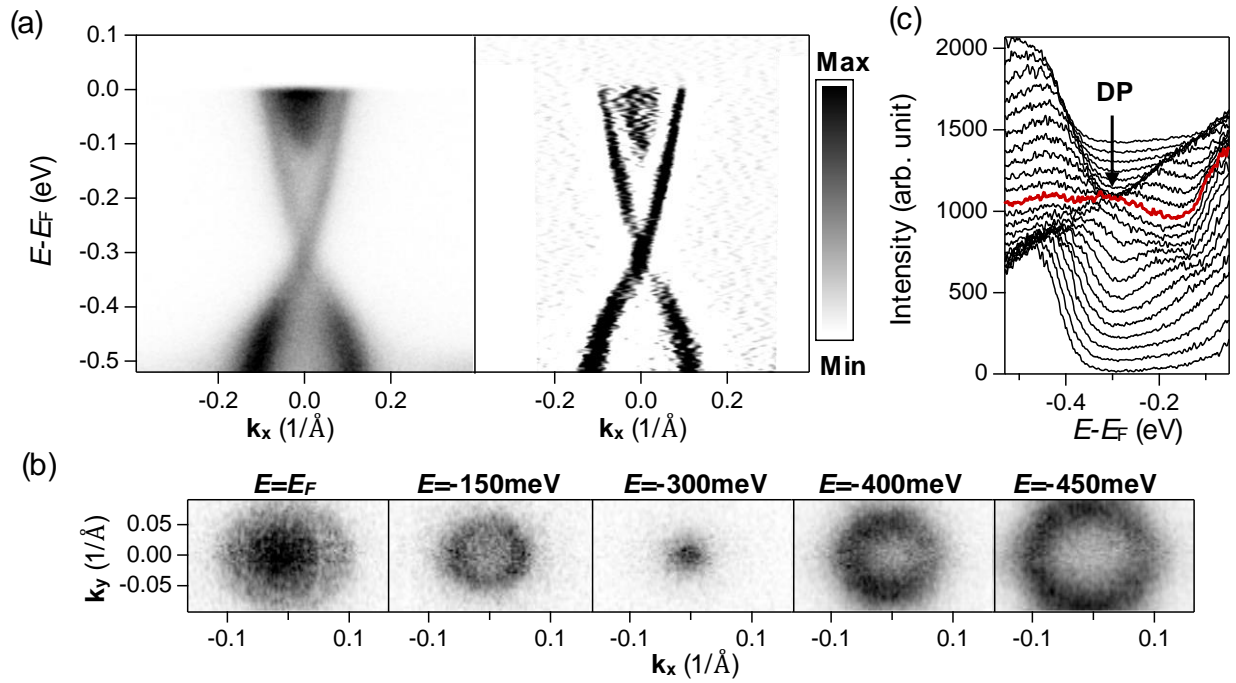


Fig. 4. Angle-resolved photo-emission spectroscopy (ARPES) spectrum and equipotential maps for a trilayer heterostructure with 8 ML Co_7Se_8 thickness. (a) ARPES spectrum cut across the Γ point along the k_x momentum direction. Left panel is the raw APRES spectrum while the right panel is the 2nd derivative of the spectrum to enhance the peak intensity of the dispersion⁴⁴. (b) Equipotential maps taken above and below the Dirac point, which is 300 meV below the Fermi level. (c) Stacking energy distribution curves (EDCs) of the ARPES spectrum in panel (a). The red curve indicates the EDC across the Dirac point (DP) at $k_x=0$.



Supplemental Materials:

Strong spin-dephasing in a topological insulator-paramagnet heterostructure

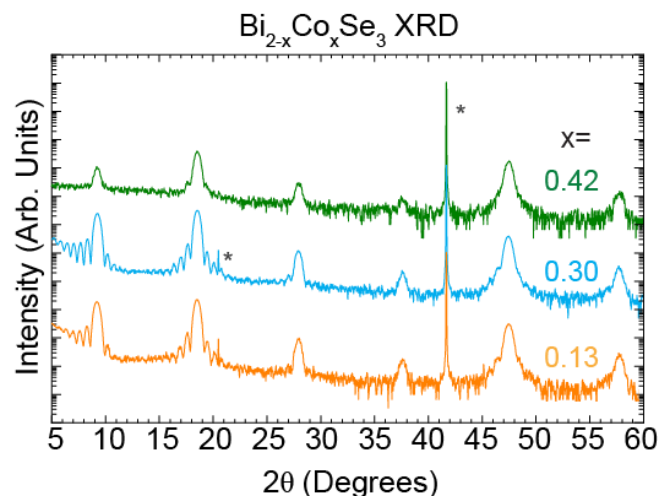
Jason Lapano¹, Alessandro R. Mazza¹, Haoxiang Li¹, Debangshu Mukherjee², Elizabeth M. Skoropata¹, Jong Mok Ok¹, Hu Miao¹, Robert G. Moore¹, Gyula Eres¹, Zac Ward¹, Ho Nyung Lee¹, Matthew Brahlek^{1*}

¹Materials Science and Technology Division, Oak Ridge National Laboratory, Oak Ridge, TN, 37831, USA

²Center for Nanophase Materials Sciences, Oak Ridge National Laboratory, Oak Ridge, TN, 37831, USA

Correspondence should be addressed to *brahlek@ornl.gov

Fig. S1. X-ray diffraction (XRD) measurements of doped $\text{Bi}_{2-x}\text{Co}_x\text{Se}_3$ series. The asterisk (*) indicates the peaks due to the Al_2O_3 substrate.



X-ray diffraction simulations of trilayer samples.

Insight into the structure of trilayer films was obtained by modeling of the specular Bragg reflections¹. The model was written in terms of out-of-plane scattering vector $q_z = 4\pi\sin(2\theta/2)/\lambda$ where for the instrument used $\lambda = 1.5406 \text{ \AA}$. The X-ray diffraction from a thin-film epitaxial sample is given by the square modulus of the sum of amplitudes from the individual layers. The specular intensity, I_{Spec} , is calculated using a kinematic model as a function of q_z and is given by

$$I_{Spec}(q_z) = \frac{S}{q_z^2} \left| \frac{F_{Sub}(q_z)}{1 - e^{-iq_z c_{Sub}}} + A_{BiSe,1}(q_z) + e^{iq_z(t_{BiSe,1} + t_{CoSe})} A_{BiSe,2}(q_z) \right|^2, \quad (1)$$

$$F_{Sub}(q_z) = \sum_{j=1}^6 \rho_O e^{iq_z(\frac{1}{12} + \frac{1}{6}j)c_{Sub}} + \rho_{Al} e^{iq_z(0.0188 + \frac{1}{6}j)c_{Sub}}, \quad (2)$$

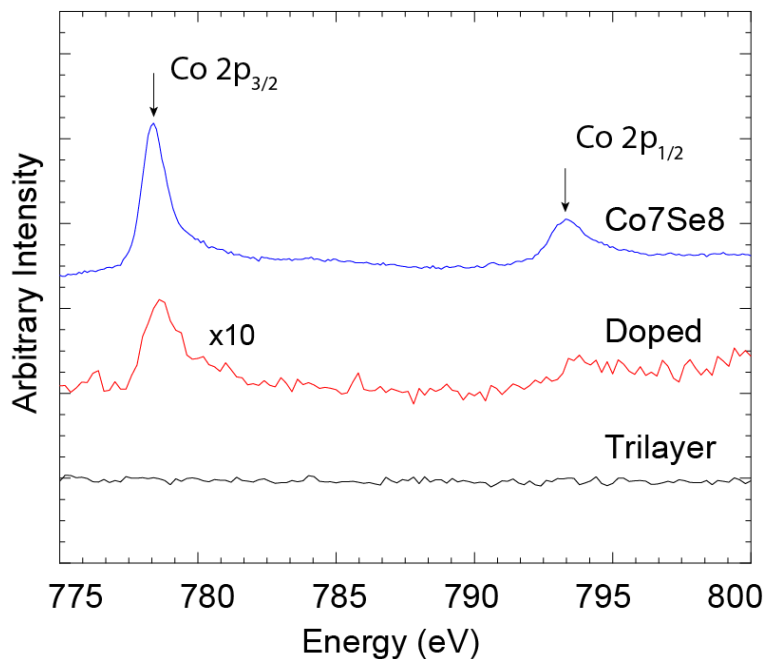
and

$$A_{BiSe,m}(q_z) = \sum_{j=0}^{n-1} \rho_{Bi} (e^{iq_z(j+0.18)d_{BiSe,m}} + e^{iq_z(j+0.56)d_{BiSe,m}}) e^{-\sigma_{j,Bi}^2 q_z^2} + \rho_{Se} (e^{iq_z(j)d_{BiSe,m}} + e^{iq_z(j+0.37)d_{BiSe,m}} + e^{iq_z(j+0.735)d_{BiSe,m}}) e^{-\sigma_{j,Se}^2 q_z^2} \quad (3)$$

where the full structure factor of the sapphire substrate is $F_{Sub}(q_z)$ and for the Bi_2Se_3 layers $A_{BiSe,m}(q_z)$, which is indexed by $m = 1$ for the bottom layer and $m = 2$ for the top layer. The parameters used are as follows:

In eq. (1) S is an overall scale factor, the term in the denominator of the for Al_2O_3 accounts for the surface truncation, and, in the third term, the phase term, $e^{iq_z(t_{BiSe,1} + t_{CoSe})}$ models the spatial separation among the two Bi_2Se_3 layers where $t_{BiSe,1}$ is the total thickness of the first Bi_2Se_3 layer and t_{CoSe} is the thickness of the equivalent Co_7Se_8 layer. In eq. (2) for Al_2O_3 $c_{Sub} = 12.991 \text{ \AA}$ is the lattice parameter along the c -axis and the terms in the parenthesis in the exponent index the atomic positions within the unit cell. For eq. (2-3) ρ_i is the atomic weight as an approximation to the atomic form factor. In eq (3), $d_{BiSe} = 9.526 \text{ \AA}$, $n = 7$ is the number of unit cells of Bi_2Se_3 , and again the terms in the parenthesis in the exponent index the atomic positions within the unit cell. For the simulation of the ideal structure the thickness of the Co_7Se_8 is 8 ML which is about 41 \AA . For the lightly mixed structure $d_{BiSe,1} = d_{BiSe}$, and $d_{BiSe,2} = 0.99 \times d_{BiSe}$, and $t_{CoSe} = 0 \text{ \AA}^2$, while the heavily mixed sample is structure $d_{BiSe,2} = 0.95 \times d_{BiSe}^2$. Finally, the exponential $e^{-\sigma_{j,Bi/Se}^2 q_z^2}$ is the Debye-Waller term that was included to account for vertical fluctuations in the atomic positions that appears as a fall off of the intensity with increasing q_z , and only changes the relative intensities of the reflections. The semiempirical parameters $\sigma_{j,Bi} = 0.001$ and $\sigma_{j,Se} = 0.01$ is related to the root-mean-square vertical displacements of atoms^{1,3}.

Fig. S2 Surface compositional analysis by X-ray photoelectron spectroscopy (XPS) performed on the 8 ML trilayer heterostructure (bottom black curve), doped sample with $x = 0.7$ (middle red curve), and Co_7Se_8 thin film (top blue curve). Cobalt is clearly visible on the surface of the doped sample and while no cobalt peak is observed for the trilayer structure, indicating the Bi_2Se_3 surface is free of Co impurities.



References

- ¹ P.F. Miceli, *Semiconductor Interfaces, Microstructures and Devices: Properties and Applications* (IOP Publishing, Bristol, 1993).
- ² M. Zhang, L. Lü, Z.-T. Wei, X.-S. Yang, and Y. Zhao, *Chinese Phys. B* **23**, 76104 (2014).
- ³ J. (Jens) Als-Nielsen and D. McMorrow, *Elements of Modern X-Ray Physics*, 2nd ed. (Wiley, 2011).